A NEW SHAPE ANALYSIS FRAMEWORK BASED ON CURVE SKELETONS

Shuisheng Xie, Jundong Liu *

School of Elec. Eng. and Comp. Sci.
Ohio University
Athens, OH 45710

Charles D. Smith

Department of Neurology
University of Kentucky
Lexington, KY 40506

ABSTRACT

Computing the average anatomy and measuring the anatomical variability within a group of subjects are common practices in Computational Anatomy. In this paper, we propose an information rich shape representation based on curve skeletons. Our method starts with the extraction of curve skeletons of the input shape, followed by fitting the object boundary with discs centered at the skeleton points. The curve skeletons and the radii of the inscribed discs are then parameterized together as the basis to represent and compare shapes. Our model has an excellent capability of capturing both global structure and local details, and the virtue of being robust to noise as well as small shape variations. Experiments with synthetic shapes and human brain structures show the effectiveness of our framework in calculating the distances among different shapes.

Index Terms— Computational Anatomy, Shape Spaces, Shape Analysis, Curve Skeleton

1. INTRODUCTION

The goal of Computational Anatomy (CA) is to estimate representative organ anatomies across diseases, populations, species or ages, to model the organ development at different spatial scales and across time (growth or aging). A common question that arises is how to compute the average anatomy as well as measure the shape variability of given a collection of anatomical images. A system that can carry out reliable group classification based on various shape structures would greatly help identify biomarker signatures of different diseases and facilitate doctors to carry out diagnosis and treatment.

1.1. Related Work

In recent years, a number of works have been published in the literature aiming to use shape spaces as the basis for subject classification. In [1], Pennec *et al.* outline a consistent computational anatomy framework for statistical measurements based on Riemannian manifold structures. Recently this framework has been applied to joint estimation and regularization of Diffusion Tensor MR Image (DTI) and to the modeling of variability of human brains [2]. Younes *et al.* [3] and Miller *et al.* [4, 5] measure population differences from a longitudinal point of view. Wang *et al.* [5] assess hippocampi change in Alzheimer's Disease (AD) using PCA and geodesic 3D evolution in estimated longitudinal deformation velocity.

Srivastava *et al.* [6, 7, 8, 9] devise a series statistical analysis methods of shapes of 2D/3D curves, facial and 3D surfaces. In [6], a novel 2D curve representation based on velocity function is proposed, together with the method to calculate the geodesics on shape spaces of closed planar curves. Generalization of this curve representation to N-dimension is introduced in [7], with a "path-straightening" as the numerical solution for geodesics computation. Three dimensional surfaces can also be handled through a collection of 3D curves [8, 9] based on the same framework. Though flexible and accurate in describing curve details, these boundary-based representations lack in capturing global shape information, and tend to be sensitive to noise. The applicability of surface models based on aggregation of 2D curves [8] are quite limited to 2.5D data, e.g. range images.

Pizer and Fletcher *et al.* [10] develop geometric representations based on the M-rep description and conduct analysis on the Riemannian space. They formulate the space of solid objects as an infinite-dimensional Riemannian manifold in which each point represents a smooth object with non-intersecting boundary. Geodesics between shapes provide a foundation for shape comparison and statistical analysis. M-rep descriptors are powerful in capturing both global and local shape variations, however, it is not a trivial task to generate them in a robust and reliable fashion.

Inspired by aforementioned works, we propose a novel curve-skeleton based shape representation and classification framework in this paper. Our method starts with the extraction of curve skeletons of the input shape, then fits the object boundary with discs centered at the skeleton points. Instead of directly parameterizing the object boundary as in [6], we parametrize curve skeletons together with the radii of the inscribed discs. Our model has the capability of capturing both global forms (e.g. bulky vs. lean; different orientations) and

*This work is in part supported by Sanders-Brown Center on Aging at University of Kentucky.

local details (e.g. blunt vs. sharp ends), and the virtue of being robust to noise as well as small shape variations.

2. SHAPE REPRESENTATION BASED ON CURVE SKELETONS

Topological skeleton is a useful shape abstraction that captures the essential topology of an object in both two and three dimensions. Skeletons can be defined as the locus of points equidistant from the contour (for 2D) or object boundary (for 3D). Alternatively, they can also be defined as the locus of centers of maximal circles in 2D, or maximally inscribed balls in 3D.

For 3D objects, the skeletons obtained from these definitions are called *surface skeletons*, which consist of a set of 2D skeletal sheets. A different type of skeleton is the *curve skeleton*, which is a collection of 1D curves locally centered with respect to the object boundary. Curve skeletons can be regarded as the medial axis of surface skeletons. While carrying the essential topology of the object, curve skeletons have a low dimensionality which makes them an ideal object representation in describing shape structures and motions, especially for "stick-figure" objects. For a genus 0 shape, its curve skeleton has the graph structure of a tree. The longest pat in the continuous curve skeleton is called *centerline*.

Generally speaking, curve skeleton extraction algorithms can be classified into two major categories, discrete methods and continuous methods. In this paper, we adopt the continuous curve skeleton & centerline extraction algorithm proposed by VanUitert and Summers [11]. Level set time-crossing map is used to compute a subvoxel precise distance field, then fast marching method is employed to propagate a front to flow along the center region of the object.

2.1. Shape Representation and Spaces

The curve skeleton of an anatomical structure bears the global information of the shape, e.g., length and orientation. The inscribed discs/balls, other the hand, tells the distance of boundary from the skeleton, therefore describes the local boundary properties. Our shape representation is the combination of the two components, and the boundary can be very well reconstructed with dense enough samples.

The curve skeleton of an anatomical shape can be parameterized as a vector-valued function $\boldsymbol{\alpha} : [0, 2\pi] \rightarrow \mathbb{R}^d$ (d is the dimension of the data) based on its arc-length s. In order for the curve to stretch, shrink and bend freely, we represent the shape of the skeleton α by the function $\boldsymbol{\beta}(s) = (\dot{\boldsymbol{\alpha}}^1(s), \dot{\boldsymbol{\alpha}}^2(s), \cdots, \dot{\boldsymbol{\alpha}}^d(s))$. Additional components can be added to enrich the information contained in the representation to describe various local shape characteristics. For example, to differentiate "bulky" and "lean" shapes, the radius of the inscribed discs (for 2D) and balls (for 3D) would obviously be a good choice. Let $\boldsymbol{\zeta}$ denote such added components, a combined representation can be obtained as follows, $\boldsymbol{\gamma} : [0, 2\pi] \rightarrow \mathbb{R}^{d+\mathfrak{d}'}$ ($\mathfrak{d}'$ is the dimension of $\boldsymbol{\zeta}$):

$$\boldsymbol{\gamma}(s) = (\boldsymbol{\beta}(s), \boldsymbol{\zeta}(s)) \tag{1}$$

In our model, $\boldsymbol{\gamma}$ will be normalized based on its standard Euclidean inner product and mapped to an infinite-dimensional unit-sphere $\mathcal{S}$. Let inner product in $\mathbb{R}^n$ be $p \cdot q$, then the inner product on $\mathcal{S}$, $< \boldsymbol{\gamma}_1, \boldsymbol{\gamma}_2 >$, is defined as:

$$< \boldsymbol{\gamma}_1, \boldsymbol{\gamma}_2 > \quad = \quad \int_0^{2\pi} \boldsymbol{\gamma}_1(s) \cdot \boldsymbol{\gamma}_2(s) ds \tag{2}$$

After $\boldsymbol{\gamma}$ is mapped onto the sphere $\mathcal{S}$ (for simplicity, we still use $\boldsymbol{\gamma}$ to denote the normalized version), the geodesics among different $\boldsymbol{\gamma}$ can be easily computed [12]. We term our model as *Information Rich shape representation based on Skeleton* (IRS) in light of the fact that additional components can be easily integrated into our representation to make it an information rich shape descriptor. Different settings of ζ would lead to IRSs with distinct capacities.

The curve skeletons of complex shapes usually contain branches, and they always take tree structures for genus 0 shapes. Correspondingly, each branch can be modeled with a single IRS and the overall shape would be represented with an IRS tree. An "importance" measure [13] can be assigned to each branch based on its influence in the entire shape, and a hierarchical analysis framework is resulted. In this paper, we focus on 2D/3D objects that can be modeled by central lines alone (no branches, or branches are insignificant therefore can to be ignored) and use radii of the inscribed discs as the additional shape representation component.

2.2. IRS for 2D Shapes

For 2D cases, the radii of the inscribed discs along the skeleton will be used as the additional representation component $\boldsymbol{\zeta}$, and the combined parameterization $\boldsymbol{\gamma}$ for an individual curve skeleton point is:

$$\boldsymbol{\gamma}(s) = (\boldsymbol{\beta}(s), R(s)/n) \in \mathbb{R}^3 \tag{3}$$

Where n is the number of points on the skeleton. We divide the radii by n to synchronize the sampling of $\boldsymbol{\beta}(s)$ and $R(s)$. The denser the samples on the skeleton, the more faithful the reconstructed shape to the original boundary.

Figure 1 illustrates the construction of an IRS. Fig. 1(a) shows a 2D shape. The reconstructed boundary (in green color) from the curve skeleton (in blue color) and inscribed discs (in red color) is shown in Fig. 1(b). As evident, the reconstructed boundary is quite close to the original input, which is an indication that our IRS, while concise, carries most of the essential information.

2.3. IRS for 3D Shapes

For a 3D object, the overall centerline of the shape is first extracted. Sampled planes perpendicular to the curve skeleton

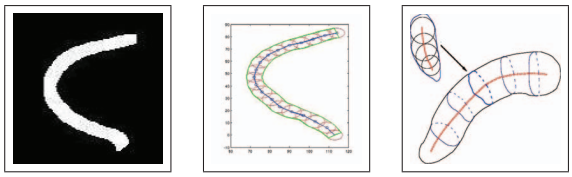

(a) (b) (c)

Fig. 1. 2D and 3D IRS representations. (a): 2D shape; (b) reconstruction from 2D IRS; (c) illustration of 3D IRS generation procedure.

are then applied to cut the 3D object into 2D cross sections. The IRS for each cross section C is formulated as

$$\boldsymbol{\gamma_{3d}}(s) = (\boldsymbol{\beta_{3d}}(s), R(s)/n) \in \mathbb{R}^4 \tag{4}$$

where β_{3d} this time is generated with the 3-dimensional points on the centerline of C (a tilted plane). Fig. 1(c) illustrates the procedure. The red dashed line is the overall centerline of the 3D object. Cross sections are obtained and modeled with $\boldsymbol{\gamma_{3d}}$ based on the individually centerlines (shown in solid red). It should be noted that the information of the overall centerline is implicitly stored in the individual cross sections.

Our IRS representation is invariant to translation and scaling, but not entirely to rotation. In order to remove rotation variability, we employ the coherent point drift algorithm (CPD) proposed by Myronenko and Song[14] to align the input shapes, before IRS computations are carried out.

3. SHAPE SPACES STATISTICS AND DISTANCE

In Euclidean space, the arithmetic mean of a point set is usually defined as the point that minimizes the sum-of-squared distances to the given points. In order to serve as a representative and best describe the average properties of the data set, the estimated mean is desired to stay in the same space as the inputs. For points on a manifold ($\mathbf{M}$), arithmetic mean calculated based on Euclidean distances are not guaranteed to remain on $\mathbf{M}$. We can enforce the inclusion by projecting the mean onto $\mathbf{M}$, but a better solution is to directly utilize the Riemmanian distance of $\mathbf{M}$ to define an *intrinsic mean* [10], which always resides on the manifold. Let $\mathbf{Exp}_p(v)$ and $\mathbf{Log}_x(y)$ denote the exponential and log maps defined on the manifold $\mathbf{M}$, and $\boldsymbol{\Gamma} = [\gamma_1, \cdots, \gamma_i, \cdots, \gamma_n]$ be the IRS representations of a group of n objects. The intrinsic mean (μ) of $\boldsymbol{\Gamma}$ can be obtained based on following Newton's iterations:

- [*Step 1*] Initialization: $\mu_0 = \gamma_{\mathbf{1}}$.
- [*Step 2*] Gradient calculation: $\Delta\mu = -\frac{1}{n}\sum_{i=1}^{n} \mathrm{Log}_{\mu_j}(\gamma_i)$
- [*Step 3*] Mean update: $\mu_{j+1} = \mathrm{Exp}_{\mu_j}(-\tau\Delta\mu)$, where τ is the step size.
- [*Step 4*] If $||\Delta\mu||$ is over a given threshold, stop and $\mu = \mu_{j+1}$. Otherwise, increase j by 1 and go to S2.

Similarily, the covariance matrix $\Sigma_{\boldsymbol{\Gamma}}$ for $\boldsymbol{\Gamma}$ can be defined based on Riemannian distance, after we map all the γ_i onto the tangent space $\mathbf{T}_\mu\mathbf{M}$:

$$\Sigma_{\boldsymbol{\Gamma}} = \frac{1}{N}\sum_{i=1}^{N} \left(\mathbf{Log}_\mu(\gamma_i)\mathbf{Log}_\mu(\gamma_i)^\top\right) \tag{5}$$

The Mahalanobis distance for a vector γ_i from the mean μ is defined as:

$$D_M(\gamma_i) = \sqrt{\mathbf{Log}_\mu(\gamma_i)^\top \Sigma_{\boldsymbol{\Gamma}}^{-1} \mathbf{Log}_\mu(\gamma_i)} \tag{6}$$

4. EXPERIMENTAL RESULTS

We conduct two groups of experiments to examine the effectiveness of our IRS model in calculating the distances among different shapes.

The first experiment is based on a group of synthetic 2D shapes. The base shape is shown in Fig. 2.(Base). Three types of transformations, "make thinner/fatter", "change orientation" and "change in the middle", have been applied to the base to obtain three groups of distorted shapes. The first row (1.1 - 1.3) shows the shapes resulted from the "make thinner/fatter" operation, with increasing magnitudes. Row 2 and 3 are the "change orientation" and "change in the middle" groups, respectively. We then ranked the distorted shapes based on their distances to the base, and the rankings are listed in the brackets next to the figure numbers. For example, (2.1) (6) means shape (2.1) is the 6-th closest to the base among all the 9 test shapes. The expectation of the rankings is that the shapes in each individual group should be ranked consistent with their distortion magnitudes, and our model obviously achieved this goal. The three data sets on row one differ from the base mainly in the radii of the inscribed discs, while the curve skeletons are kept almost identical to that of the base. Comparing with (1.2), (1.1) and (1.3) are much thinner and fatter, so they are reasonably ranked behind (1.2). Same logic applies to the three data sets on row 3. The row 2 data sets go through a gradual orientation change, which makes them really "different" from the base shape.

Second group of experiments use data provided by Sanders Brown Center on Aging at the University of Kentucky (UK-COA). T1-weighted structural MR images from the Alzheimer's Disease Neuroimaging Initiative (ADNI) project were segmented using FSL/FIRST tool, and the segmented Thalami were used as the structures of interest. The first two rows in Fig 3 show five segmented Thalami and the corresponding extracted curve skeletons + cutting cross sections. The central column is zoomed in for better view. We then fitted the Thalami using our 3D IRS representation, and the mean cross sections were computed based on the 4-step procedure outlined in the section **3**. Mean curve skeleton was obtained through a group registration procedure based

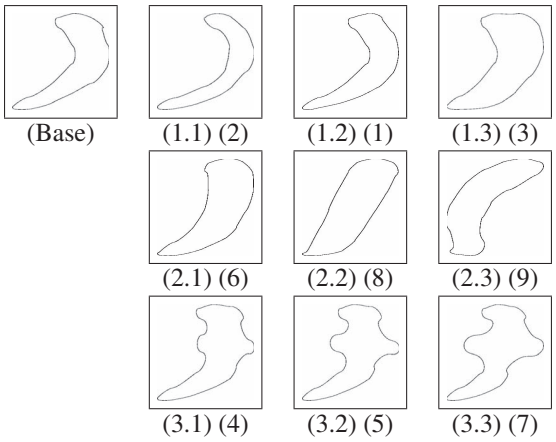

Fig. 2. Ranking shapes based on the distance measure. Refer to text for details.

on the CPD algorithm [14]. Fig. 3(a) shows the five extracted curve skeletons (in blue color) together with the mean skeleton (in red color). Fig. 3(b) shows one particular group of cross sections and the estimated group mean (in red color). The mean cross sections together with the mean skeleton are shown in Fig. 3(c). The excellent discriminative capability of our model demonstrated from the experiments would be the foundation to develop a reliable shape classification system.

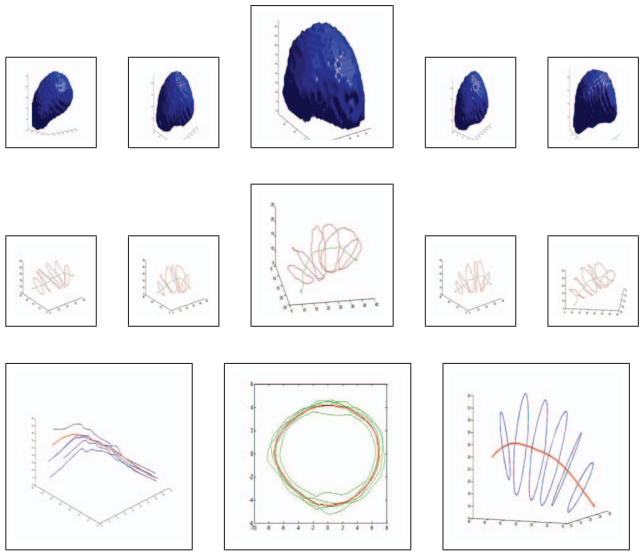

Fig. 3. First row: five segmented Thalami. Second row: the extracted curve skeletons and cross sections. Third row: (a) average curve skeleton; (b) one group of cross sections and the group mean; (c) average cross sections.

5. REFERENCES

[1] Xavier Pennec, "Probabilities and statistics on riemannian manifolds: Basic tools for geometric measurements," in *NSIP99*, June 20-23, Antalya, Turkey, 1999, IEEE-EURASIP, vol. 1, pp. 194–198.

[2] S. Durrleman, P. Thompson X. Pennec, A Trouvé, and N. Ayache, "Inferring brain variability from diffeomorphic deformations of currents: an integrative approach," *Medical Image Analysis*, vol. 12, no. 5, pp. 626–637, 2008.

[3] Laurent Younes, "Jacobi fields in groups of diffeomorphisms and applications," *Quarterly Journal of Applied Math*, vol. 65, no. 1, pp. 113–134, 2006.

[4] Anqi Qiu, Christine Fennema-Notestine, Anders M. Dale, and Michael I. Miller, "Regional shape abnormalities in mild cognitive impairment and alzheimer's disease," *NeuroImage*, vol. 45, no. 3, pp. 656 – 661, 2009.

[5] Lei Wang et al., "Large deformation diffeomorphism and momentum based hippocampal shape discrimination in dementia of the alzheimer type," *IEEE Trans. Med. Imaging*, vol. 26, no. 4, pp. 462–470, 2007.

[6] Eric Klassen, Anuj Srivastava, Washington Mio, and Shantanu H. Joshi, "Analysis of planar shapes using geodesic paths on shape spaces," *IEEE Trans. Pattern Anal. Mach. Intell.*, vol. 26, no. 3, pp. 372–383, 2003.

[7] Shantanu H. Joshi, Eric Klassen, Anuj Srivastava, and Ian Jermyn, "A novel representation for riemannian analysis of elastic curves in r^n," in *CVPR*. 2007, IEEE Computer Society.

[8] Anuj Srivastava, Chafik Samir, Shantanu H. Joshi, and Mohamed Daoudi, "Elastic shape models for face analysis using curvilinear coordinates," *Journal of Mathematical Imaging and Vision*, vol. 33, no. 2, pp. 253–265, 2009.

[9] Sebastian Kurtek, Eric Klassen, Zhaohua Ding, and Anuj Srivastava, "A novel riemannian framework for shape analysis of 3d objects," in *CVPR*. 2010, pp. 1625–1632, IEEE.

[10] P. Thomas Fletcher, Conglin Lu, Stephen M. Pizer, and Sarang C. Joshi, "Principal geodesic analysis for the study of nonlinear statistics of shape," *IEEE Trans. Med. Imaging*, vol. 23, no. 8, pp. 995–1005, 2004.

[11] Robert L. Van Uitert Jr. and Ronald M. Summers, "Automatic correction of level set based subvoxel precise centerlines for virtual colonoscopy using the colon outer wall," *IEEE Trans. Med. Imaging*, vol. 26, no. 8, pp. 1069–1078, 2007.

[12] R. Ferreira, J. Xavier, J.P. Costeira, and V. Barroso, "Newton method for riemannian centroid computation in naturally reductive homogeneous spaces," in *ICASSP 2006*, may 2006, vol. 3, p. III.

[13] Dennie Reniers, Jarke J. van Wijk, and Alexandru Telea, "Computing multiscale curve and surface skeletons of genus 0 shapes using a global importance measure," *IEEE Trans. Vis. Comput. Graph.*, vol. 14, no. 2, pp. 355–368, 2008.

[14] Andriy Myronenko and Xubo B. Song, "Point set registration: Coherent point drift," *IEEE Trans. Pattern Anal. Mach. Intell.*, vol. 32, no. 12, pp. 2262–2275, 2010.